



## Template-free mesoporous $\text{La}_{0.3}\text{Sr}_{0.7}\text{Ti}_{1-x}\text{Fe}_x\text{O}_{3 \pm \delta}$ for $\text{CH}_4$ and CO oxidation catalysis

Buğra Kayaalp<sup>a,1</sup>, Siwon Lee<sup>b,1</sup>, Kurt Klauke<sup>a</sup>, Jongsu Seo<sup>b</sup>, Luca Nodari<sup>c,d</sup>, Andreas Kornowski<sup>e</sup>, WooChul Jung<sup>b,\*</sup>, Simone Mascotto<sup>a,\*</sup>

<sup>a</sup> Institut für Anorganische und Angewandte Chemie, Universität Hamburg, Martin-Luther-King-Platz 6, D-20146, Hamburg, Germany

<sup>b</sup> Department of Materials Science and Engineering, Korea Advanced Institute of Science and Technology, 291 Daehak-ro, Yuseong-gu, Daejeon, 34141, Republic of Korea

<sup>c</sup> Istituto di Chimica della Materia Condensata e di Tecnologie per l'Energia, ICMATE-CNR, C.so Stati Uniti 4, Padova, 35127, Italy

<sup>d</sup> Dipartimento di Scienze Chimiche, Università di Padova, Via Marzolo 1, Padova, 35131, Italy

<sup>e</sup> Institut für Physikalische Chemie, Universität Hamburg, Grindelallee 117, D-20146 Hamburg, Germany



### ARTICLE INFO

#### Keywords:

Perovskite  
SOFC  
VOC  
Structural stability  
Reaction mechanism

### ABSTRACT

The design of perovskite oxides with improved textural properties in combination with tunable composition variations is a forward-looking strategy for the preparation of next generation catalytic converter. In the present work we report the template-free synthesis of mesoporous solid solutions of  $\text{La}_{0.3}\text{Sr}_{0.7}\text{Ti}_{1-x}\text{Fe}_x\text{O}_{3 \pm \delta}$  ( $0 \leq x \leq 0.5$ ) and the study of their catalytic performance towards  $\text{CH}_4$  and CO oxidation. Using an innovative polymer complex route, phase pure perovskite solid solutions with specific surface area of  $65 \text{ m}^2 \text{ g}^{-1}$  and average pore size of 15 nm were prepared. The iron concentration increase led to a progressive enhancement of not only both concentration and transport of the charge carriers but also reducibility and oxygen desorption capability on the catalyst. As a result, we observed almost complete conversion of  $\text{CH}_4$  and CO at 600 °C and 300 °C, respectively. Kinetic studies on methane oxidation showed that competing *suprafacial* and *intrafacial* reaction mechanisms coexist, and that the concentration of 30% of Fe maximizes the *suprafacial* contribution. Under reducing conditions at 600 °C the materials retained their structural and morphological integrity, showing superior stability. Finally, the reaction rate of  $\text{CH}_4$  and CO conversion evidenced that our systems are by a maximum of 90 times more performing than other bulk and nanoporous Fe-based perovskites in literature (e.g.  $\text{La}_{0.66}\text{Sr}_{0.34}\text{Co}_{0.2}\text{Fe}_{0.8}\text{O}_{3-\delta}$ ), as a result their large surface area, intimate gas-solid contact and short intragrain oxygen diffusion pathways induced by the mesoporous structure.

### 1. Introduction

The growing demand for efficient power generation systems with minimized emission of pollutants is at the moment a major driving force pushing for the development of cost-effective, non-toxic, stable and active catalyst materials. In this respect perovskite oxides are currently experiencing a renaissance in many fields of the energy sector from Li-batteries [1] to solar fuels [2,3], fuel cells [4] and diesel soot combustion [5]. It is well known that the versatility of this class of materials is given by their ease in accommodating nonstoichiometry without compromising their structural stability. The rational introduction of doping species in A and/or B position of the perovskite lattice is a feature largely exploited for the design of the materials for energy conversion devices, because it significantly influences their ionic and electronic mobility as well as electronic structure. Along with the optimization of the composition, the improvement of the morphological

properties of the oxides is a further essential requirement for such applications. In comparison to nanoparticulate systems, nanoporous materials possess higher concentration of active sites thanks to their larger specific surface area. In particular, the realization of well-connected networks of mesopores, i.e. pores between 2 and 50 nm, is highly desired, because the size related enhancement of the pore wall adsorption potential improves the fluid-solid interactions. Furthermore, the existence of mesoscaled pore walls guarantees short intragrain diffusion pathways favoring the transport of ionic and electronic charge carriers. Hence, the design of perovskite oxides, which combine mesoporosity with controlled cationic substitution, represents an ultimate goal for the development of high performance catalytic devices [6].

Even though the preparation of nanoporous and mesoporous perovskite oxide powders is meanwhile reported by several wet-chemistry studies [7–12], to the best of our knowledge, the simultaneous

\* Corresponding authors.

E-mail addresses: [wcjung@kaist.ac.kr](mailto:wcjung@kaist.ac.kr) (W. Jung), [simone.mascotto@chemie.uni-hamburg.de](mailto:simone.mascotto@chemie.uni-hamburg.de) (S. Mascotto).

<sup>1</sup> These authors equally contributed to the realization of this work

substitution of both lattice positions within a mesoporous structure has not been described yet. Most of the synthetic protocols proposed thus far rely on the impregnation of colloidal crystals or mesoporous silica [7,11–13], used as structure directing agents to impart the wanted porosity. As the concentration of the metal precursor solution in the confined geometry of the hard template needs to be maximized, the larger is the number of the cations the harder is to guarantee the generation of a homogeneous, single phase, highly substituted perovskite structure. In addition, these standard approaches are prolonged, multi-step procedures. They often require harsh conditions for the template removal (e.g. concentrated NaOH solutions), inevitably affecting the chemical nature of the perovskite surface and their use for catalytic applications.

A solid solution between strontium titanate and strontium ferrite,  $\text{Sr}(\text{Ti},\text{Fe})\text{O}_{3-\delta}$ , has attracted since years considerable attention in many applications such as solid oxide fuel cell electrodes [14–20], electrochemical membranes for partial oxidation of hydrocarbons [21–23], oxygen permeation membranes [24,25], lean burn exhaust sensors [26,27], and hydrocarbon gas sensors [28,29], due to its high mixed ionic/electronic conductivity and favorable reactivity to various gases. However, these promising functions can be hindered by the poor chemical stability of the material both in highly reducing conditions and also with respect to reaction with common solid-electrolyte materials such as yttrium-stabilized zirconia (YSZ) [30,31]. To address this issue, Fagg et al. have reported the replacement substitution of Sr on the A-site by La to significantly improve the material's phase stability and chemical compatibility with YSZ [32]. Furthermore, La acting as a donor also leads to an increase in the electronic conductivity under reducing atmospheres [33,34]. Thus, given also the excellent tolerance of the oxide itself against coking and sulfur poisoning, a  $(\text{La},\text{Sr})(\text{Ti},\text{Fe})\text{O}_{3-\delta}$  (LSTF) system can be a promising ceramic anode material for solid oxide fuel cells using hydrocarbon fuels [35,36]. Despite many relevant studies [32,35,36], there are surprisingly few works on LSTF as a chemical catalyst, with fewer yet being reported for their reactivity to hydrocarbon conversion via oxidants (e.g., oxygen, steam, carbon dioxide) [36].

Herein we present the template-free synthesis of mesoporous  $\text{La}_{0.3}\text{Sr}_{0.7}\text{Ti}_{1-x}\text{Fe}_x\text{O}_{3\pm\delta}$  ( $0 \leq x \leq 0.5$ ) materials and investigate their catalytic properties towards  $\text{CH}_4$  and CO oxidation. Inspired by our recent work on mesoporous  $\text{SrTiO}_3$  [9], this paper reports the single-step preparation of mesoporous  $\text{La}_{0.3}\text{Sr}_{0.7}\text{Ti}_{1-x}\text{Fe}_x\text{O}_{3\pm\delta}$  solid solutions with large surface area ( $65 \text{ m}^2 \text{ g}^{-1}$ ) and porosity ( $0.2 \text{ cm}^3 \text{ g}^{-1}$ ). Besides the superior material morphology, homogeneous distribution of the ions within a phase pure perovskite lattice is observed. Combining X-ray diffraction, Mössbauer spectroscopy, electrochemical impedance spectroscopy (EIS) along with temperature programmed desorption (TPD) and reduction (TPR), we demonstrate that as the Fe content increases, the reducibility and the ability to desorb oxygen of the material are markedly improved. Furthermore, we demonstrate that Fe is a key reaction site to activate both surface and bulk oxygen species needed for  $\text{CH}_4$  oxidation, and two different reaction pathways coexist for the reaction over LSTF catalysts surface: *suprafacial* vs. *intrafacial* mechanism. As a result of the mutual benefit of the improved textural and redox properties, the solid solutions showed much higher catalytic activity towards the oxidation of CO and  $\text{CH}_4$  than bulk and standardly templated porous perovskite catalysts reported in the literature (e.g.  $\text{LaFeO}_3$  [37–40],  $\text{LaCo}_{0.6}\text{Fe}_{0.4}\text{O}_3$  [38],  $\text{La}_{0.8}\text{Sr}_{0.2}\text{FeO}_3$  [40] and  $\text{La}_x\text{Sr}_{1-x}\text{M}_y\text{Fe}_{1-y}\text{O}_{3-\delta}$  ( $\text{M} = \text{Co, Ni}$ ) [41]), while maintaining good thermal stability. These observations provide sound understanding of the gas-phase reaction at LSTF surface and present the potential of a novel synthesis route towards highly substituted perovskite oxides as high-temperature chemical and electrochemical catalysts.

## 2. Experimental

### 2.1. Materials

Strontium nitrate (99%, Acros Organics), titanium (IV) isopropoxide (98%, ABCR), iron (III) nitrate nonahydrate (reagent grade, Merck), lanthanum (III) nitrate hexahydrate (99.9%, Alfa Aesar), anhydrous citric acid

(99.6%, Acros Organics), glycerol (99%, Alfa Aesar) and glacial acetic acid (HOAc 99%, VWR) were used as received without further purification.

### 2.2. Synthesis of mesoporous $\text{La}_{0.3}\text{Sr}_{0.7}\text{Ti}_{1-x}\text{Fe}_x\text{O}_{3\pm\delta}$

Porous  $\text{La}_{0.3}\text{Sr}_{0.7}\text{Ti}_{1-x}\text{Fe}_x\text{O}_{3\pm\delta}$  (LSTF) systems were prepared by chelate complex route. In a typical synthesis, the stoichiometric amount (5.43–2.72 mmol) of titanium (IV) isopropoxide was added to 11.9 mL glycerol. After 30 min of stirring, 40.7 mmols of citric acid was added. The mixture was heated to 60 °C and stirred for 1 h at this temperature to ensure the complete dissolution of citric acid. Subsequently, 3.80 mmols  $\text{Sr}(\text{NO}_3)_2$  dissolved in 1.0 mL deionized water, 1.63 mmols  $\text{La}(\text{NO}_3)_3 \cdot 6\text{H}_2\text{O}$  and stoichiometric amount (0–2.72 mmol) of  $\text{Fe}(\text{NO}_3)_3 \cdot 9\text{H}_2\text{O}$  were added respectively at 30 min intervals under continuous stirring. Finally, the solution was stirred further for 2 h and then the temperature was raised to 130 °C. The polycondensation reaction between the chelating agents was then achieved under vigorous stirring for 2 h. The resulting polymer gel was calcined in air with a heating ramp of  $2^\circ\text{C min}^{-1}$ . 2 h holding time each was implemented at intermediate and final temperature steps of 400 °C and 600 °C respectively. The resulting perovskite oxide powder was then washed with glacial acetic acid (1.0 M) to eliminate carbonate impurities [42]. Samples were named on the basis of the mol % substitution of Fe in the perovskite, where  $x = 0.1$  in  $\text{La}_{0.3}\text{Sr}_{0.7}\text{Ti}_{1-x}\text{Fe}_x\text{O}_{3\pm\delta}$ , corresponds to LSTF10 and  $x = 0.5$  corresponds to LSTF50.  $\text{SrTiO}_3$  and  $\text{La}_{0.3}\text{Sr}_{0.7}\text{TiO}_{3+\delta}$  compositions are referred as STO and LSTO.

### 2.3. X-ray diffraction

X-ray diffraction (XRD) analyses were carried out with an X'Pert Pro diffractometer (PANalytical Corp.) with 1.5406 Å Ni-filtered Cu-K $\alpha$  radiation, operating at 45 kV and 40 mA. The mean crystallite sizes were calculated from the full width at half maximum (FWHM) of the most intense reflection (110) using the Scherrer equation.

### 2.4. Mössbauer spectroscopy

Room Temperature Mössbauer spectroscopy was performed on a conventional constant acceleration spectrometer mounting a Rh matrix  $^{57}\text{Co}$  source, nominal strength 1850 MBq. The hyperfine parameters are compiled on Table S1. The spectra were fitted to Lorentzian line shapes with the minimum number of components. 8 is quoted relative to standard  $\alpha$ -Fe foil.

### 2.5. Nitrogen physisorption

The nitrogen sorption isotherms were obtained at 77 K using a Quadasorb SI-MP by Quantachrome. Outgassing was performed with a Masterprep Degasser (Quantachrome Corp.) at 120 °C for 12 h. Specific surface areas were determined with the Brunauer–Emmett–Teller (BET) method [43] at  $p/p_0 = 0.07$ –0.3. Pore size distribution was determined with the NLDFT method [44] applying the model for cylindrical pores on the adsorption branch by using the Quantachrome ASiQWin software.

### 2.6. Electron microscopy

Transmission electron microscopy (TEM) measurements were carried out on a JEOL JEM 2200 FS operating at 200 kV equipped with two CEOS Cs correctors (CETCOR, CESCOR), a JEOL JED-2300 Si(Li) EDX (energy dispersive X-ray spectroscopy) detector, a Gatan 4 K UltraScan 1000 camera and a HAADF (high angle annular dark field) detector. The sample was grinded into a fine powder, which was suspended in toluene by sonication and dropped on a carbon coated 400 mesh TEM grid. The excess of solvent was removed with a filter paper and by drying the grid under air.

EDX mapping was acquired using  $256 \times 256$  pixels (pixel size of 0.7 nm) and a dwell time of  $0.5 \text{ ms pixel}^{-1}$  (corrected for dead time) with 30 cycles. Additionally, EDX measurements were repeated at least

on three positions for each sample and less than 1.0 at. % disparity was observed for surveyed cations at each point.

### 2.7. X-ray photoelectron spectroscopy

The surface chemical nature of the prepared  $\text{La}_{0.3}\text{Sr}_{0.7}\text{Ti}_{1-x}\text{Fe}_x\text{O}_{3\pm\delta}$  powder was analyzed by X-ray photoelectron spectroscopy using a Sigma probe (Thermo Scientific, USA) under ultrahigh vacuum environment with a 400  $\mu\text{m}$ -diameter beam of monochromatic X-ray source, Al  $\text{K}\alpha$  ( $\hbar\nu = 1486.6$  eV) radiation. To obtain detail information of oxygen, high-resolution XPS scans of oxygen 1s were carried out.

### 2.8. TPR/ $H_2$

The temperature-programmed reduction measurements under a  $H_2$  environment ( $H_2$ -TPR) were performed with a Micromeritics AutoChem 2920 analyzer. The catalyst ( $\sim 100$  mg) was pretreated under 5%  $O_2$  stream balanced in He (50 mL min $^{-1}$ ) at 550 °C for 2 h. After the sample cooled to 150 °C, a flow of 5%  $H_2$  in He gas (50 mL min $^{-1}$ ) was introduced into the samples at a flow rate of 50 mL min $^{-1}$ , and the temperature was increased to 650 °C at a heating rate of 10 °C min $^{-1}$ . The amount of consumed  $H_2$  was measured using a thermal conductivity detector (TCD).

### 2.9. TPD/ $O_2$

The temperature-programmed desorption analyses of oxygen ( $O_2$ -TPD) were conducted on a Micromeritics AutoChem 2920 analyzer. Before TPD, each sample ( $\sim 100$  mg) was pretreated under 5%  $O_2$  balanced in He (50 mL min $^{-1}$ ) at 550 °C for 2 h. After cooling to 150 °C, the TPD operation was carried out under a He carrier gas (30 mL min $^{-1}$ ) from 150 °C to 650 °C at a heating rate of 10 °C min $^{-1}$ . The amount of oxygen desorbed was monitored by a thermal conductivity detector (TCD).

### 2.10. Impedance spectroscopy

The as-prepared powders (0.3 g) were uniaxially pressed into disks with 13 mm in diameter and 1 mm thickness at 222 MPa. The samples were subsequently heated to 600 °C for 2 h, resulting in stable disks. Electrodes were applied to both sides of the disks using colloidal silver paste (Plano GmbH).

Impedance measurements were performed using a Novocontrol Alpha A impedance analyzer connected to a NorECs Probostat® sample chamber. A Novocontrol-HT controller connected to a type S thermocouple mounted next to the sample was employed for temperature control. Frequencies between 10 $^{-2}$  Hz and 10 $^7$  Hz were employed with an amplitude of 10 mV<sub>rms</sub> for all measurements. Novocontrol WinFIT was used for data evaluation and equivalent circuit fitting. The sample resistance was obtained from the (RQ) elements not corresponding to the electrode response. Due to the porous structure of the samples no further analysis regarding grain boundary and bulk contributions was carried out. The oxygen partial pressure (4% oxygen atmosphere) was set by mixing Ar with synthetic air using MKS MF-1 mass flow controllers. The oxygen partial pressure was verified using a NorECs miniature oxygen sensor electrode with a sealed internal metal/metal oxide reference and a Rigol DM-3058 multimeter. A constant gas flow of 19 sccm was employed for all measurements with the gas supply tube ending in close proximity to the sample. All samples were first equilibrated overnight at 500 °C and the desired partial pressure. Each temperature was held for 2 h before a measurement was performed.

### 2.11. $CH_4$ and CO oxidation

The catalytic activities for  $CH_4$  and CO oxidation were measured in a fixed-bed quartz flow micro-reactor with an internal diameter of 4 mm. For all the measurements we used 100 mg catalyst mixed with 100 mg quartz sand and loaded in-between two plugs of quartz wool for preventing displacement of the catalyst. The feed of methane oxidation (composed of 2 vol

%  $CH_4$ , 4 vol%  $O_2$  in Ar) and carbon monoxide oxidation (composed of 1 vol %  $CO$ , 4 vol%  $O_2$  in Ar) was flowed into the reactor. The total flow rate was adjusted for both oxidation reactions to 50 mL min $^{-1}$ . The reactant and product gases were monitored in real time with a quadrupole mass spectrometer (PFEIFFER Vacuum GSD320) connected to the reactor outlet. The light-off curve was measured with a ramping rate at 3 °C min $^{-1}$ , after activating the catalysts in the reaction atmosphere up to 600 °C for methane oxidation and 300 °C for CO oxidation. The  $CH_4$  and  $CO$  conversion ratio (%) were defined as  $100 \times (\text{mol } CH_4, \text{ in} - \text{mol } CH_4, \text{ out})/\text{mol } CH_4, \text{ in}$ , and  $100 \times (\text{mol } CO, \text{ in} - \text{mol } CO, \text{ out})/\text{mol } CO, \text{ in}$ , respectively. In order to determine the reaction order for  $CH_4$  and  $O_2$ , we investigated the reaction rate by varying the partial pressure of methane (from  $2 \times 10^{-3}$  to  $6 \times 10^{-3}$  atm) while keeping the partial pressure of oxygen constant ( $5 \times 10^{-2}$  atm). In the same way, we observed the reaction rate according to the partial pressure change of oxygen (from  $1 \times 10^{-2}$  to  $5 \times 10^{-2}$  atm) while keeping the partial pressure of methane ( $2 \times 10^{-3}$  atm) the same. The signal of  $CH_4$  was detected by the  $m/z = 15$  peak instead of the 16 peak (the major peak of methane) to avoid the contribution caused by the cracking fragment of carbon monoxide (0.9%), water (1.1%), carbon dioxide (8.5%), and oxygen (11%). The signal of  $CO$  was corrected for the contribution from the cracking fragment of  $CO_2$  (11.4%) with mass concentration determination mode.

### 2.12. TG-MS

The stability of material in reducing atmosphere was tested using a NETZSCH STA 449F3 coupled over a capillary with Aeolos QMS403C (TG – MS) setting a 5 °C min $^{-1}$  heating rate up to 600 °C in an Ar/ $H_2$  stream (volume ratio 90/10). Another batch of the material was heated up to 600 °C in a muffle furnace under air atmosphere with 5 °C min $^{-1}$  heating rate and a hold time of 1 h. The evaluation of the structure subsequent to the heat treatment under reducing and oxidizing atmospheres was realized with XRD and  $N_2$  physisorption.

## 3. Results and discussion

The textural properties of the prepared  $\text{La}_{0.3}\text{Sr}_{0.7}\text{Ti}_{1-x}\text{Fe}_x\text{O}_{3\pm\delta}$  (LSTF) systems were assessed by nitrogen physisorption analysis. Each LSTF system showed similarly high BET surface areas of  $\sim 65 \text{ m}^2 \text{ g}^{-1}$  and pore volumes of  $\sim 0.2 \text{ cm}^3 \text{ g}^{-1}$  (Table 1). Obtained curves could be characterized as type IV(a) isotherms, indicating the clear presence of a mesoporous structure (Fig. 1a) [45]. The pore size distribution (PSD) analysis points to a quite narrow distribution of mesopores with an average of ca. 15 nm. Majority of the pores had 7–17 nm diameter, whereas larger pores of up to 30 nm were present at low amounts (Fig. S1). The substantial surface areas and porosities can be ascribed to the choice of glycerol as co-monomer in the polymer synthesis (Fig. S2) [46]. Compared to the commonly used ethylene glycol, this polyol enables superior crosslinking between the polyester chains. As can be seen by the TEM analyses, this entangled system during thermal treatment likely induces the formation of mesoporous oxide particle aggregates (Fig. 1b). All LSTF systems were comprised of crystalline aggregates of several micrometers featuring disordered pores of approx. 15 nm, in very good agreement with physisorption analyses (Fig. S3, Fig. S4a). High resolution images and their corresponding FFT representations (Fig. 1b inset, Fig. S4b) show the presence of single phase nanocrystallites of approx. 25 nm size. Notably, this mesoporous architecture of LSTF provides an extremely high specific surface area for facile gas-phase reaction and enables ideally percolated channels for electric current as well as gas flow.

EDX spectroscopy from TEM was employed to investigate the local composition of the solid solutions. Experimental values concur with the nominal stoichiometric amounts of the  $\text{La}_{0.3}\text{Sr}_{0.7}\text{Ti}_{1-x}\text{Fe}_x\text{O}_{3\pm\delta}$  general formula (Table 1). For each sample elemental mapping at high magnification shows highly homogeneous distribution of elements over the particles (Fig. S5), excluding the existence of any impurity phase.

XRD analyses show that all systems present a single phase cubic perovskite structure with space group Pm-3 m and average crystallite size of

**Table 1**

Crystallite sizes ( $\Phi$ ) retrieved from XRD, specific surface area ( $S_{\text{BET}}$ ) and pore volume ( $V_p$ ) determined by  $N_2$  physisorption, average atomic composition of elements determined by EDX (at. % values normalized by total nominal cation amount in  $\text{La}_{0.3}\text{Sr}_{0.7}\text{Ti}_{1-x}\text{Fe}_x\text{O}_{3 \pm \delta}$  molecular formula), and composition of different Fe sites retrieved by Mössbauer spectroscopy for investigated LSTF systems from 0 to 50 mol % Fe substitution on B-site.

Sample	$\Phi$ [nm]	$S_{\text{BET}}$ [ $\text{m}^2 \text{g}^{-1}$ ]	$V_p$ [ $\text{cm}^3 \text{g}^{-1}$ ]	La	Sr	Ti	Fe	$\text{Fe}^{3+}$ (1) [%]	$\text{Fe}^{3+}$ (2) [%]	$\text{Fe}^{4+}$ [%]
LSTO	22	54	0.21	0.29	0.72	1.00	—	—	—	—
LSTF10	27	63	0.19	0.29	0.74	0.84	0.13	59	41	—
LSTF30	25	65	0.20	0.34	0.65	0.67	0.34	60	36	4
LSTF50	22	59	0.23	0.29	0.70	0.55	0.53	60	30	10

25 nm (Fig. 1c and Table 1), in very good agreement with TEM. The shift of the (110) reflection depicted on Fig. 1d can be explained by the counter-balancing of lattice constant expansion and contraction effects from  $\text{La}^{3+}$  and  $\text{Fe}^{3+}$  respectively. Substitution of  $\text{Sr}^{2+}$  ( $r = 1.44 \text{ \AA}$ ) by the smaller  $\text{La}^{3+}$  ( $r = 1.36 \text{ \AA}$ ) generates shrinkage of the unit cell, which is again expanded when Fe is inserted into the structure up to 30 mol %. This widening is justified by the substitution of  $\text{Ti}^{4+}$  ( $r = 0.605 \text{ \AA}$ ) by  $\text{Fe}^{3+}$  ( $r = 0.645 \text{ \AA}$ ). Further shrinkage observed at higher concentration of iron could be associated with the formation of the smaller  $\text{Fe}^{4+}$  species ( $r = 0.585 \text{ \AA}$ ), usually found in STF solid solutions [47,48]. Better understanding of the local environment of the B-site substituent Fe was obtained by Mössbauer

spectroscopy measurements. The spectra show a similar central absorption, typical of iron nuclei in paramagnetic regime (Fig. 2a). The best fit for the curve of LSTF10 was achieved by two octahedral ferric sites (see Table S1 and Fig. S6) which can be ascribed to the existence of two different symmetrical environments arising from Sr-, La- double substitution on the A site, in good agreement with other findings [49,50]. Enhancing the concentration of iron in the system, the relative amount of  $\text{Fe}^{3+}$  on site 2 decreases in favor of the formation of  $\text{Fe}^{4+}$  species [49]. This population increased up to 10% of the total Fe amount in LSTF50 (Table 1), thus explaining the lattice contraction observed in the XRD patterns (Fig. 1d).

Analysis of the conductive behavior of the different solid solutions was

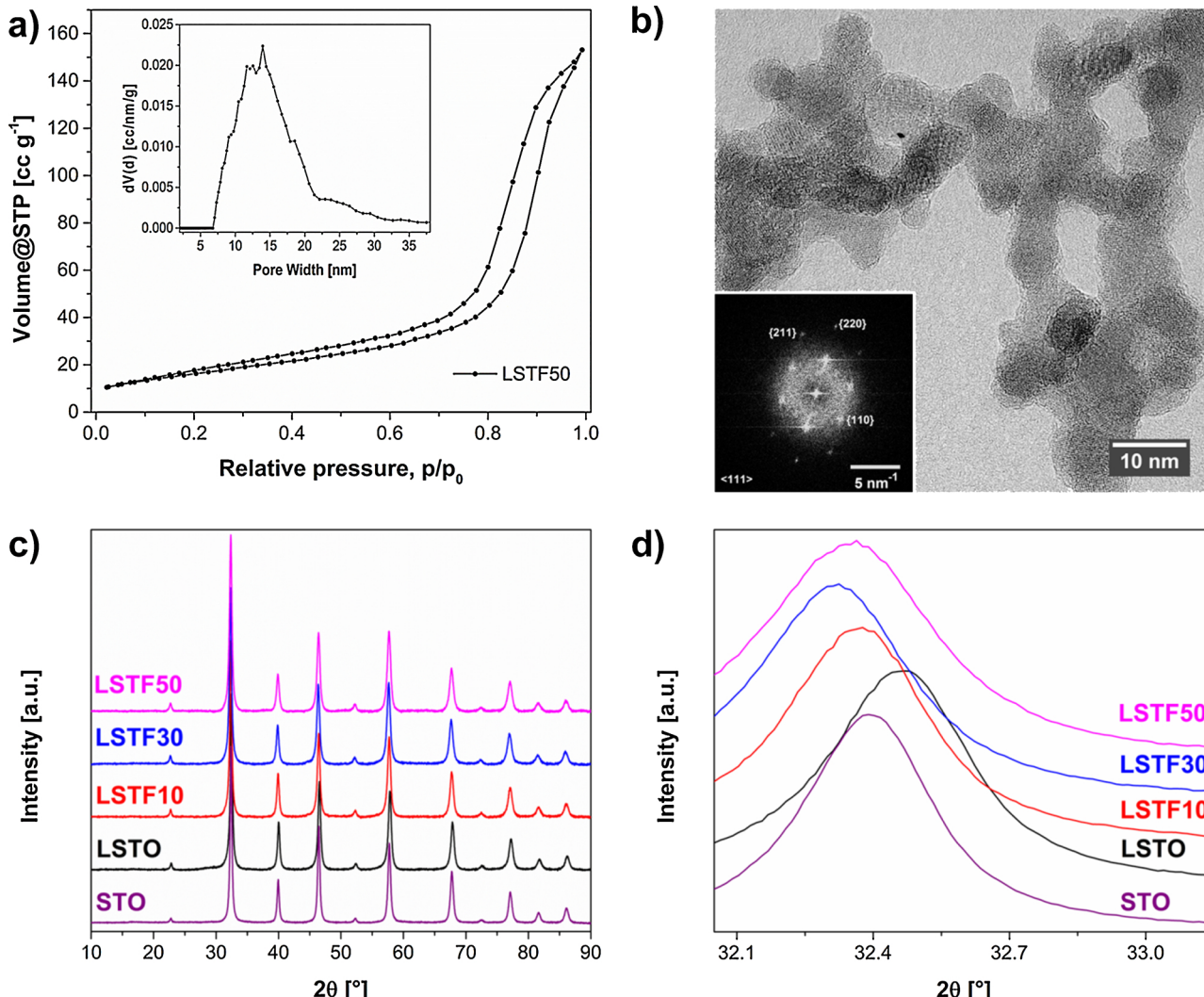


**Fig. 1.** (a) Nitrogen physisorption isotherm and pore size distribution (inset) and (b) TEM micrograph of LSTF50 chosen as representative system and FFT representation of a single crystallite (inset). (c) X-ray diffraction patterns of pure STO phase and LSTF systems from 0 to 50 mol % Fe substitution on B-site. The shift of the (110) reflection (d) illustrates the contraction of lattice by  $\text{La}^{3+}$  substitution on A-site (STO – LSTO) following expansion by  $\text{Fe}^{3+}$  substitution on B-site (LSTO – LSTF30) and finally contraction due to the developing  $\text{Fe}^{4+}$  (LSTF30 – LSTF50).

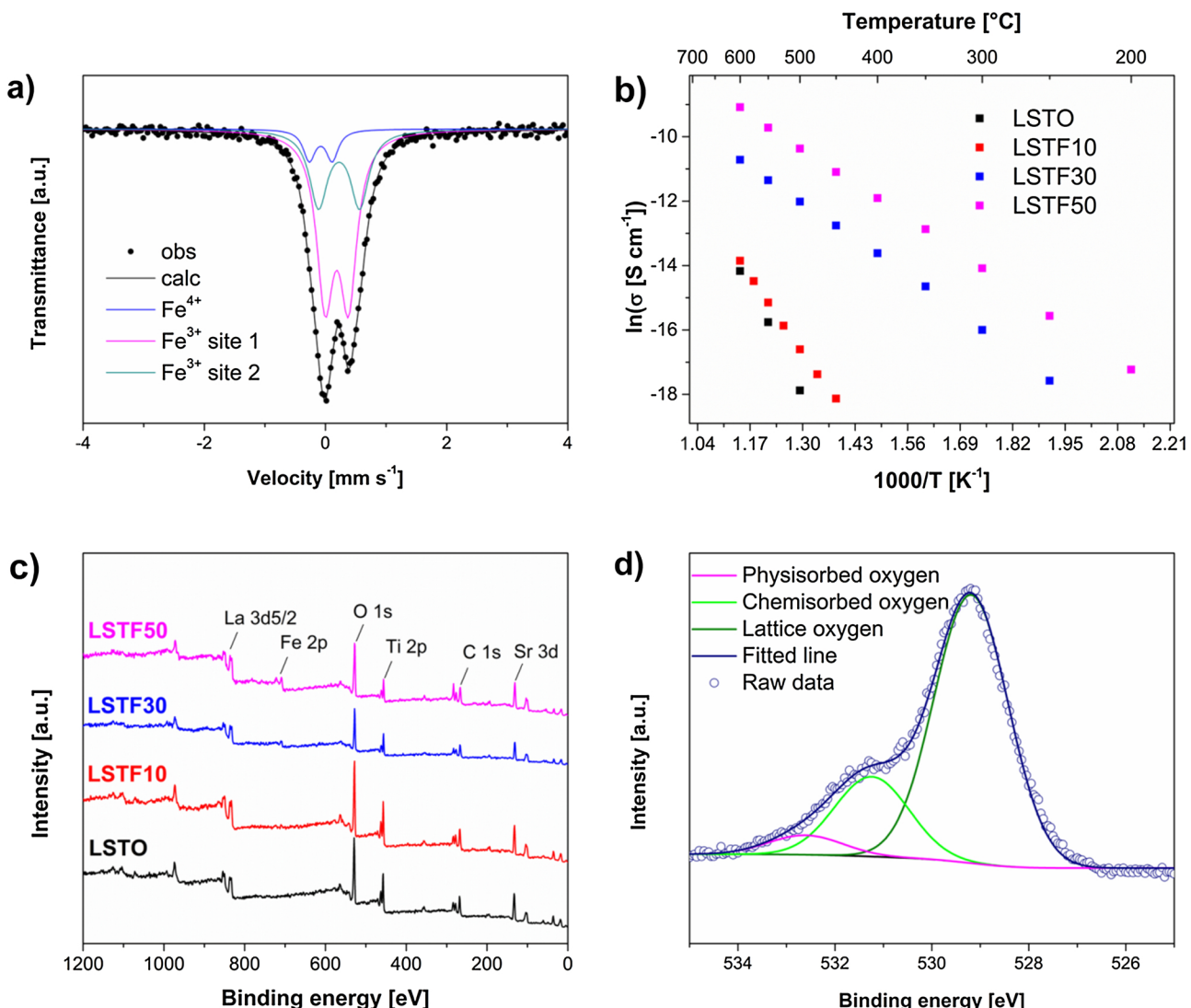


**Fig. 2.** (a) Mössbauer Spectrum of LSTF50 chosen as representative system and fitting of Fe-sites (b) Arrhenius plots of the conductivity and (c) XPS survey over the surface of LSTF systems from 0 to 50 mol % Fe substitution (d) O 1s region of the XPS spectrum obtained for LSTF50 and fitting of the different oxygen species.

determined by means of electrochemical impedance spectroscopy (EIS) at 4% oxygen atmosphere. From the Arrhenius plots in Fig. 2b one can see a progressive increase in total conductivity. Taking into account that porosity and grain size do not vary significantly between different compositions (See Table 1 and Fig. S3), the improved conductivity is attributed to the higher iron content. This is consistent with the fact that the progressive substitution of the tetravalent Ti centers by trivalent Fe is compensated at the measuring conditions by the increasing generation of electronic and ionic charge carriers, such as electron holes, oxygen vacancies and oxygen interstitials [17,51]. The activation energy (Table 2) of charge migration, obtained by the curve slope, decreases up to 30 mol % of iron content. For larger iron concentrations, the overall conductivity increases due to higher charge carrier density, however the transport mechanism remains the same as for LSTF30, thus explaining the constant activation energy. The significant change of the transport behavior between LSTF10 and LSTF30 is related to charge compensation phenomena in LSTF systems. According to Perry et al. [52], in oxidizing conditions, as those adopted here, Sr substitution by La mainly induces the formation of interstitial oxygen. For  $[Fe] \ll [La]$  the oxygen vacancy formation as a consequence of the B-site substitution will be then suppressed and with it the charge transport. However, under  $[Fe] \geq [La]$  conditions the concentration of free vacancies will be restored and the charge carries mobility enhances. The changes in the nature of LSTF surface with increasing Fe-substitution was investigated

by X-ray photoelectron spectroscopy (Fig. 2c). All elements could be identified on the surface in accordance with the elemental ratios determined from EDX analysis (Table S2). Upon analysis of the O1s region shown in Fig. 2d, three components could be identified at around 529, 531 and 532 eV, attributed to lattice oxygen, chemisorbed and physisorbed oxygen species respectively [53,54]. The relative amounts of chemisorbed oxygen species which are bound to surface oxygen vacancies, increased progressively with increasing Fe-substitution (Fig. 2d, Fig. S7).

$H_2$ -TPR and  $O_2$ -TPD experiments were conducted on the LSTF systems to investigate their redox properties, which are key factors determining the catalyst performance. The resulting profiles are illustrated in Fig. 3 and the amounts of consumed hydrogen and released oxygen are reported in Table 2. The TPR was performed to obtain information on the reducibility of the oxides as well as the heterogeneity of the reducible characteristics, particularly focusing on surface  $Fe^{4+}$  and  $Fe^{3+}$  species. For iron-free LSTO sample, only a broad peak, which is attributed to the reduction of  $Ti^{4+}$  to  $Ti^{3+}$ , above 650 °C is present. On the other hand, several reduction steps were observed for the Fe-substituted samples. The initial signal at ~260 °C observed both in LSTF30 and LSTF50 systems is attributed to the reduction of  $Fe^{4+}$  to  $Fe^{3+}$  [55,56]. The absence of peaks at 260 °C for the system with 10 mol % Fe-substitution confirms the findings of Mössbauer spectroscopy that no  $Fe^{4+}$  sites are present for LSTF10. The three peaks between 300–650 °C can be assigned to the

**Table 2**

Activity parameters of LSTF catalysts. H<sub>2</sub>-TPR: Hydrogen consumption obtained from temperature programmed reduction experiments. O<sub>2</sub>-TPD: Oxygen desorption obtained from temperature programmed desorption experiments.  $E_a^{EIS}$ . Activation energy for charge migration obtained by electrochemical impedance spectroscopy.  $E_a^{CO\ ox.}$ ,  $E_a^{CH_4\ ox.}$ : Activation energy for CH<sub>4</sub> and CO oxidation reactions over LSTF catalysts obtained below 10% conversion.  $m$ ,  $n$ : Empirically calculated reaction orders  $m$  with respect to CH<sub>4</sub> and  $n$  with respect to O<sub>2</sub> obtained below 10% CH<sub>4</sub> conversion (reaction rate =  $kP_{CH_4}^m P_{O_2}^n$ ), SRR: *Suprafacial* reaction rate dependent on the contribution of  $\alpha$ -oxygen. IRR: *Intrafacial* reaction rate dependent on the contribution of  $\beta$ -oxygen. IRR and SRR were obtained at 510 °C with  $p_{CH_4} = 0.002$ ,  $p_{O_2} = 0.03$  atm. TRR: Total reaction rate.

Sample	H <sub>2</sub> -TPR [mmol g <sup>-1</sup> ]	O <sub>2</sub> -TPD [μmol g <sup>-1</sup> ]	$E_a^{EIS}$ [kJ mol <sup>-1</sup> ]	$E_a^{CO\ ox.}$ [kJ mol <sup>-1</sup> ]	$E_a^{CH_4\ ox.}$ [kJ mol <sup>-1</sup> ]	$m$	$n$	SRR (x 10 <sup>-8</sup> ) [mol g <sub>cat</sub> <sup>-1</sup> s <sup>-1</sup> ]	IRR (x 10 <sup>-8</sup> ) [mol g <sub>cat</sub> <sup>-1</sup> s <sup>-1</sup> ]	TRR (x 10 <sup>-8</sup> ) [mol g <sub>cat</sub> <sup>-1</sup> s <sup>-1</sup> ]
LSTO	0.43	1.5	—	92	134	0.71	0.39	0.806	0.266	1.07
LSTF10	0.72	9.4	150	64	109	0.73	0.26	4.06	3.30	7.36
LSTF30	1.26	38.3	74	56	92	0.68	0.14	11.2	43.9	55.1
LSTF50	1.31	108.6	70	66	90	0.76	0.02	4.73	73.2	77.9

gradual reduction of Fe<sup>3+</sup> to Fe<sup>2+</sup> [55,57]. The disparity in intensity can be ascribed to occupation of different local lattice environments as shown by Mössbauer spectroscopy with increasing Fe amount in the structure. Finally, the signal appearing between 650–750 °C for the LSTF samples are attributable to the reduction of Ti<sup>4+</sup>, even though reduction of Fe<sup>2+</sup> to Fe<sup>0</sup> cannot be excluded in this temperature region [55–57].

The oxygen mobility of LSTF systems were analyzed by monitoring the oxygen evolution during temperature-programmed desorption (O<sub>2</sub>-TPD) experiments. Generally, perovskite oxides are known to desorb two types of oxygen. One is the alpha oxygen ( $\alpha$ -oxygen) that is desorbed from the weakly adsorbed oxygen species on the surface in the relatively low-temperature region (< 500 °C) and the other one is the beta-oxygen ( $\beta$ -oxygen) that is originated from the tightly bonded lattice oxygen released at high temperatures (> 500 °C) [58–60]. As shown in Fig. 3b, for Fe-free LSTO sample, only oxygen desorption above 600 °C is observed, which is therefore attributed to the desorption of  $\beta$ -oxygen. Similar tendency was also observed for Fe-substituted catalysts. However, with increasing amount of iron, the onset temperature was reduced from 600 °C to 400 °C and the intensity of the corresponding signal was increased. Since this signal is associated with the lattice oxygen, the evolution of this oxygen species indicate that the more the Fe substitutes for Ti, the easier it is to release oxygen from the perovskite lattice, as confirmed by other studies [47,48]. Moreover, LSTF materials all showed a low-temperature peak, which can be ascribed to  $\alpha$ -oxygen. Parallel to the increase in chemisorbed oxygen amounts observed by XPS, the  $\alpha$ -oxygen peak position shifted to lower temperatures with increasing Fe amount, from ~400 °C for LSTF10 to ~260 °C for LSTF50. Unfortunately, it was difficult to separate the  $\alpha$  and  $\beta$  oxygen contribution to the total amount of desorbed oxygen only with O<sub>2</sub>-TPD result due to the continuous release of oxygen species according to the temperature. Instead, we can observe that the total amount of desorbed oxygen per unit mass increases steadily from 1.46 μmol g<sup>-1</sup> for LSTO up to

108.55 μmol g<sup>-1</sup> with increasing Fe-substitution (Table 2). The high reducibility and oxygen desorption capability observed thus far suggest that LSTF can act as a good oxidation catalyst [47,56,61]. To confirm this, we investigated CH<sub>4</sub> and CO oxidation over the LSTF solid solutions. With respect to CH<sub>4</sub> oxidation, reaction over STO and LSTO reference perovskite without any Fe species led to a comparable conversion of ~10% at 600 °C (See Fig. S8). It can be deduced that catalytic activity remains relatively unaffected by substitution of La on the A site up to 30 mol %. Fig. 4a shows CH<sub>4</sub> conversion ratio over LSTF catalysts as a function of reaction temperature. The reaction products in each case have been solely H<sub>2</sub>O and CO<sub>2</sub> pointing to complete oxidation of methane. From the conversion ratio plots, it is clear that as Fe content increases, CH<sub>4</sub> is oxidized more actively. For example, more than 30 mol % of Fe on B-site yields about 90% conversion, whereas CH<sub>4</sub> conversion sharply decreases to 27 and 8% as the Fe content decreases to 10 mol % to 0 mol %, respectively. The remarkable difference between the extents of methane conversion over LSTF10 and LSTF30 is most probably related to oxygen vacancies suppression in LSTF10 as a result of the larger concentration of La<sup>3+</sup> with respect to Fe<sup>3+</sup> as explained in the discussion of the EIS results. The apparent activation energies ( $E_a^{CH_4\ ox.}$ ,  $E_a^{CH_4\ ox.}$ ) for CH<sub>4</sub> oxidation, calculated from the Arrhenius type plots shown in Fig. 4b, were compiled in Table 2. It is noted that all the rate measurements were conducted below the 10% conversion ratio region to observe the intrinsic material properties. The Fe-free sample (LSTO) shows a relatively high  $E_a$  of 134 kJ mol<sup>-1</sup>, but all other Fe-substituted samples (LSTF) have almost similar  $E_a$  values between 90 to 106 kJ mol<sup>-1</sup>. This observation indicates that CH<sub>4</sub> oxidation is highly dependent on the presence of Fe, and a similar reaction mechanism is operative for a series of LSTF catalysts containing Fe species. In methane combustion, water vapor being present either as adducts in the feed gas or products of reaction may influence the catalytic activity. Therefore, we conducted the methane oxidation activity measurements in the presence of water vapor (1.2 vol%) for the

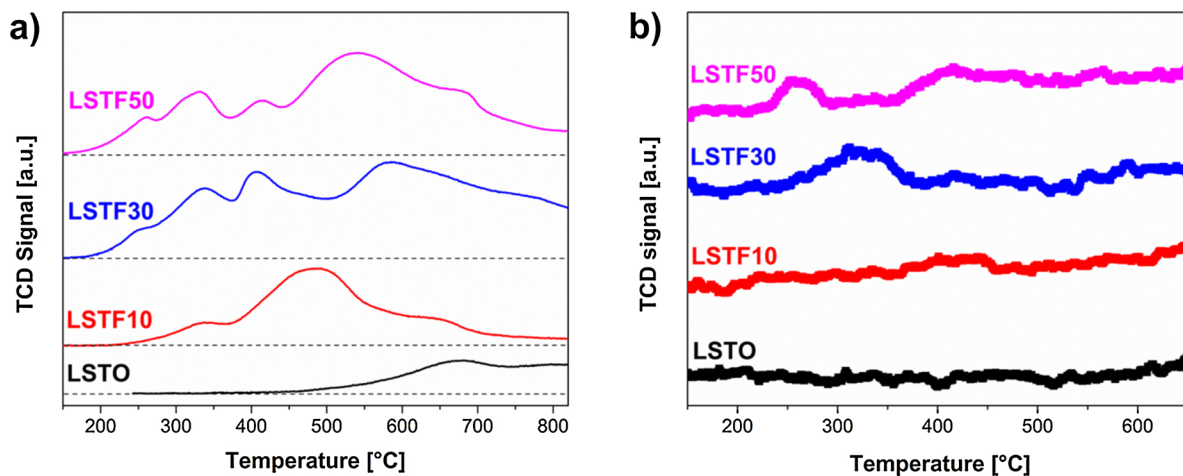
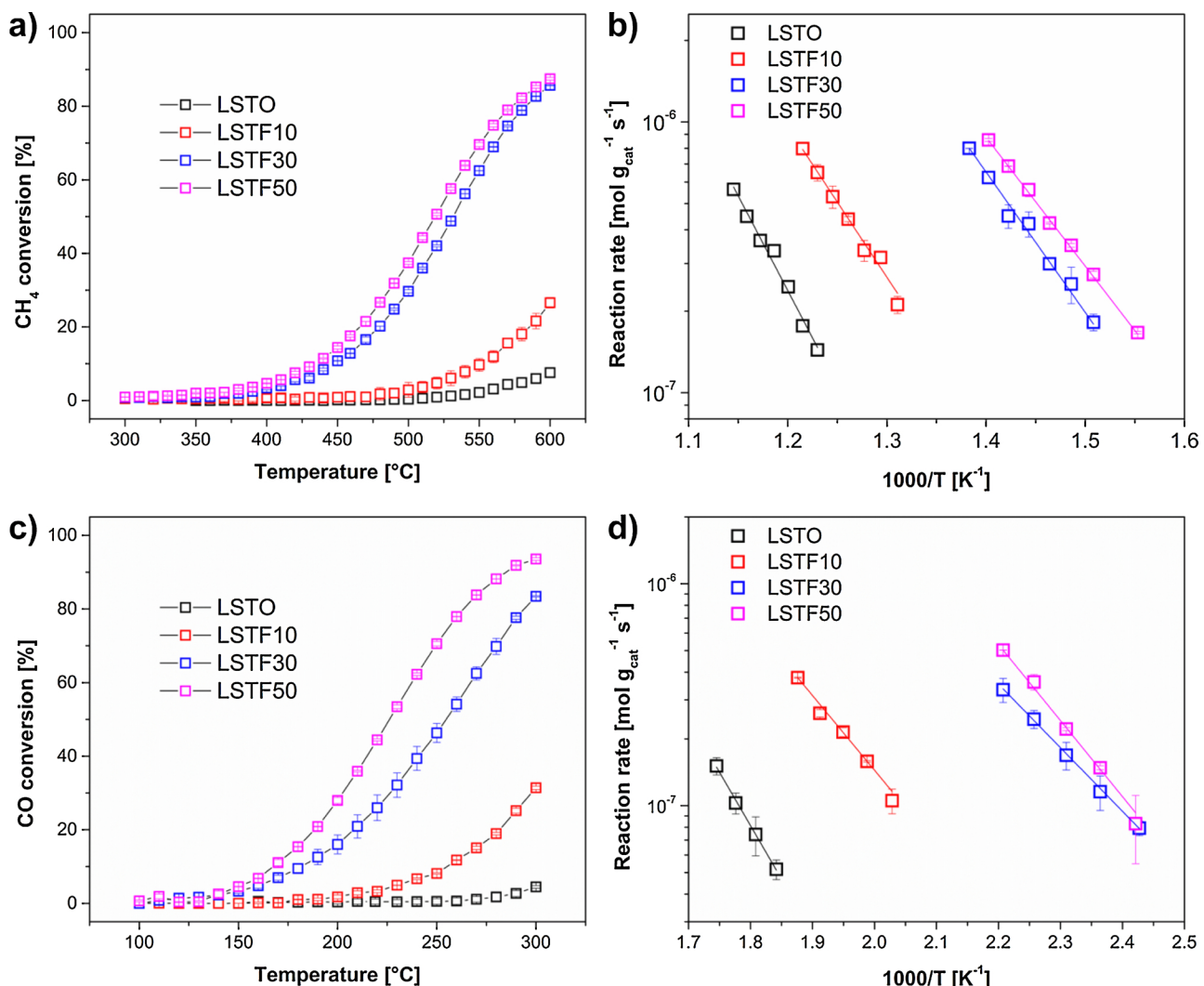


Fig. 3. (a) Temperature programmed reduction (TPR-H<sub>2</sub>) (b) and temperature programmed desorption (TPD-O<sub>2</sub>) profiles of LSTF systems from 0 to 50 mol % Fe substitution. Curves are shifted by offsets for clarity, dashed lines correspond to the baselines of each curve.



**Fig. 4.** Steady state conversions obtained for the oxidation reaction of CH<sub>4</sub> (a) and oxidation reaction of CO (c) over LSTF samples and pertaining Arrhenius plots respectively for CH<sub>4</sub> oxidation (b) and CO oxidation (d).

La<sub>0.3</sub>Sr<sub>0.7</sub>Ti<sub>1-x</sub>Fe<sub>x</sub>O<sub>3±δ</sub> catalysts (Fig. S9). The feed-gas containing water vapor was introduced into the catalyst at a temperature of 450, 500, or 550 °C for 60 min, and then, water-vapor free reactants were supplied for another 60 minutes. We observed the decrease in catalytic activity for all the samples regardless of the amount of Fe species in the catalyst. The inactivation of catalyst was reversible and the reaction rate of CH<sub>4</sub> oxidation recovered completely when water vapor supply was halted. This phenomenon is in agreement with the previous studies [62,63]. In such systems, the inhibition of catalyst by water vapor is due to the competitive adsorption of H<sub>2</sub>O and O<sub>2</sub> on the catalyst surface where the adsorption of H<sub>2</sub>O is stronger than that of O<sub>2</sub>. As shown in Fig. S9, the decrease in conversion rate was below 2 times of reaction rate for all samples when the temperature was above 500 °C. Thus, this result confirms that the addition of H<sub>2</sub>O does not greatly affect the conversion rate on our catalyst at above 500 °C.

To investigate the catalytic oxidation properties of LSTF samples in a low temperature oxidation reaction, we also carried out CO oxidation reaction test. Similar to the results of CH<sub>4</sub> oxidation reactivity test, reaction over STO and LSTO reference perovskite without any Fe species led to a comparable conversion of ~5% at 300 °C (Fig. S9) and CO was oxidized more actively as Fe content increased (Fig. 3c). The kinetic rate data indicates that the  $E_a^{CO\text{ox}}$  values of LSTO sample shows higher energy barrier of 92 kJ mol<sup>-1</sup> than the  $E_a^{CO\text{ox}}$  values of LSTF samples (Fig. 4d and Table 2), showing similar trend to the kinetic results for methane oxidation. Hence, the catalysis results pointed out that the activation energy is

not affected significantly by the amount of Fe substitution, while oxidation catalytic activity is increased as more Fe species involved. This behavior indicates the so-called compensatory effect [61], the higher conversion is due to an increase in the number of active sites rather than enhancement of the activity for the individual reaction sites, which in turn it is reflected in a larger pre-exponential factor. Therefore, considering all the experimental results together (XRD, Mössbauer spectroscopy, H<sub>2</sub>-TPR, O<sub>2</sub>-TPD and oxidation catalysis), it can be established that Fe species are indeed highly related to the active site for oxidation catalysis in the LSTF system.

To determine the dependence of the methane oxidation reaction on the reacting O<sub>2</sub> and CH<sub>4</sub> species, kinetic studies were performed. Reaction orders for CH<sub>4</sub> and O<sub>2</sub> allow us to investigate the role of oxygen species depending on the Fe-content in CH<sub>4</sub> oxidation reaction (Table 2). Using the empirical rate equation,

$$r = kP_{CH_4}^m P_{O_2}^n \quad (1)$$

where  $r$  is the reaction rate,  $k$  the rate constant,  $P_{CH_4}$  and  $P_{O_2}$  are the methane and oxygen partial pressures with  $m$  and  $n$  the respective reaction orders, we found that the reaction order for methane ( $m$ ) is about 0.7, regardless of the amount of Fe-loading. The positive value of reaction order for CH<sub>4</sub> (theoretically first-order) indicates that methane supply is not sufficient during surface reaction. This may be due to the weak adsorption characteristics of methane on the catalyst surface, however, as we observed,

the loading amount of Fe does not significantly affect to the adsorption characteristics of  $\text{CH}_4$  species. On the other hand, the reaction order ( $n$ ) for oxygen diminishes from 0.46 to 0.01 as the amount of Fe increases. This means that the supply of oxygen becomes sufficient during the catalytic reaction with higher Fe content, suggesting that Fe can promote the activation of oxygen. This gradual reduction of  $P_{\text{O}_2}$  dependence can be interpreted using a kinetic model that describes the situation in which two different reactions occur simultaneously [62,63]:

$$r = k_s P_{\text{CH}_4} (K_{\text{O}_2} P_{\text{O}_2})^{1/2} + k_i P_{\text{CH}_4} \quad (2)$$

where  $r$  represents again the reaction rate,  $k_s$  the rate constant for *suprafacial* mechanism,  $k_i$  the rate constant for *intrafacial* mechanism and  $K_{\text{O}_2}$  the oxygen adsorption equilibrium constant. The first term ( $k_s P_{\text{CH}_4} (K_{\text{O}_2} P_{\text{O}_2})^{1/2}$ ) describes that loosely adsorbed oxygen species ( $\alpha$ -oxygen) are mainly involved in the reaction (*suprafacial* mechanism). The half order kinetics of oxygen partial pressure ( $P_{\text{O}_2}$ ) are characteristic of the reaction, and the effect of strongly bound lattice oxygen is negligible. The second term ( $k_i P_{\text{CH}_4}$ ) represents that tightly entangled lattice oxygen ( $\beta$ -oxygen) is dominantly reactive during the high-temperature oxidation (*intrafacial* mechanism), where the reaction rate exhibits the zero order characteristic to oxygen partial pressure. However, because of the simultaneous contribution of both *suprafacial* and *intrafacial* mechanisms during methane oxidation, the measured empirical reaction order ( $n$ ) for oxygen in perovskite oxides is not always proportional to  $P_{\text{O}_2}$  with a power-law exponent of 1/2 or 0, as observed in our result [62,64].

In this study, we successfully separate the contribution of each oxygen species using the two-term kinetics model (Fig. S10). The observed reaction rates follow the kinetic model very well, which suggest that two different reaction paths coexist on the LSTF surface. The contribution of each oxygen species were compiled in Table 2 and plotted in Fig. 5. As the Fe content increases, the participation of  $\beta$ -oxygen increases gradually in methane oxidation, especially when the Fe content exceeds 30%, the contribution of  $\beta$ -oxygen becomes more active. However, the contribution of  $\alpha$ -oxygen increases until the Fe content reaches 30 mol %, and then slightly decreases with more Fe content. This may be due to a dilution effect, that is isolated Fe ions formed at lower Fe concentration are more active than Fe species surrounded by oxygen bound to other Fe ions [37]. Slightly lower activation energy observed for CO oxidation over LSTF30 further implies the presence of this phenomenon.

As the content of Fe is lower in LSTF catalysts, the *suprafacial* mechanism seems to be more important on the overall reaction rate, whereas the *intrafacial* mechanism becomes dominant at higher Fe concentration. Nonetheless, it is clear that the sum of reaction rates by two active oxygen species increases as the Fe content increases in LSTF catalyst, thereby it is apparent that higher substitution of Fe on the B-site would be better to achieve high catalytic activity. However, there should be inevitable structural instability of the catalyst with more Fe, so that it is important to ensure high catalytic activity while securing phase stability with low Fe content. Our experimental results demonstrate that the incorporation of 30 mol % of Fe can maximize the dilution effect and thus improve the participation of  $\alpha$ -oxygen, giving comparable reaction rate with LSTF50 sample. Furthermore, enhanced phase stability is expected in LSTF30 sample due to the high amount of Ti species in the catalyst.

To confirm the superior catalytic properties of the mesoporous LSTF presented in this work, we compared the oxidation performance of the LSTF30 and LSTF50 samples with those of other ferrite perovskites reported in literature by means of turnover frequency (TOF) values on Fig. 6. The chosen systems were both bulk and porous, the latter ones prepared by standard templating procedures. In this study, TOF was defined as the reaction rate normalized by the total number of Fe species, which is considered to be an active site in LSTF catalysts. We found that both LSTF30 and 50 samples showed higher  $\text{CH}_4$  and CO conversion activity by maximum 90 times at 560 °C and 300 °C, respectively. This remarkable result depends not only on the extremely high specific surface area of our samples,

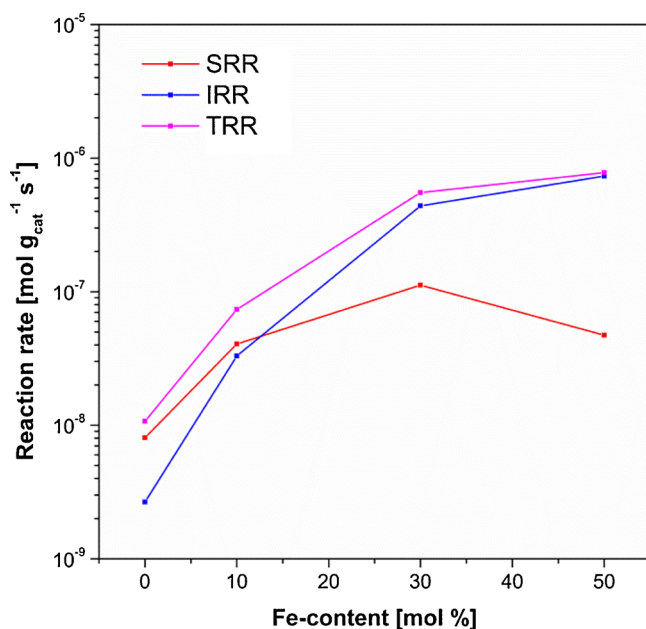


**Fig. 5.** Change in *suprafacial* reaction rate (SRR) governed by  $\alpha$ -oxygen and *intrafacial* reaction rate (IRR) governed by  $\beta$ -oxygen with variations in Fe content. TRR corresponds to the total reaction rate.

but also on the unique mesoporous structure which guarantees intimate gas-solid contact and short diffusion pathways for the reactive oxygen species to reach the grain surface during reactions. In addition to their excellent catalytic activities, the LSTF catalysts can be also deemed to be significantly more robust than the  $\text{LaFeO}_3$  or  $\text{SrFeO}_{3.8}$  perovskites, as significant amount of stabilizing  $\text{Ti}^{4+}$  species is present on the B-site [32]. The structural and morphological stability of our catalysts was evaluated by treating the material in reducing and oxidizing atmospheres at 600 °C for 1 h. The XRD and  $\text{N}_2$  physisorption analyses subsequent to the heating treatment revealed no change in porosity, phase purity and microstructure, demonstrating the potential of these materials for high-temperature applications such as IT-SOFCs and hydrocarbon reforming catalysis (Figs. S11–S12).

#### 4. Conclusions

In this work the synthesis of mesoporous solid solutions of  $\text{La}_{0.3}\text{Sr}_{0.7}\text{Ti}_{1-x}\text{Fe}_x\text{O}_{3\pm\delta}$  ( $0 \leq x \leq 0.5$ ) and the study of their catalytic performance towards  $\text{CH}_4$  and CO oxidation is presented. Phase pure cubic perovskite oxides with specific surface area of  $65 \text{ m}^2 \text{ g}^{-1}$  and average pore size of 15 nm could be obtained independent of their iron content using an innovative template-free polymer complex approach. The iron concentration increase prompted the formation of  $\text{Fe}^{4+}$  species in the material and led to a progressive improvement of the ionic and electronic charge carrier activity. We could show that the higher is the reducibility of the materials the higher is their oxygen supply as a result of charge compensation mechanism. Two types of oxygen species were delivered, namely  $\alpha$ -oxygen and  $\beta$ -oxygen, indicating desorption from the loosely and tightly bound oxygen on the oxide, respectively. Catalytic oxidation studies evidenced improved performance with increasing iron content with a maximum of 90% conversion of methane at 600 °C and carbon monoxide at 300 °C. Kinetic studies of methane oxidation demonstrated that two competing reaction mechanisms coexist (*suprafacial* and *intrafacial*) in which the concentration of 30% of Fe maximizes the contribution of *suprafacial* mechanism and is suitable to give high oxidation reactivity with minimal compromise on structural stability. Moreover, after treating the materials in reducing atmospheres we showed that not only the crystalline phase but also the porous characteristics remained unaffected, demonstrating the superior structural and morphological stability of our catalysts. More importantly, the comparison of the  $\text{CH}_4$  and CO reaction rate with

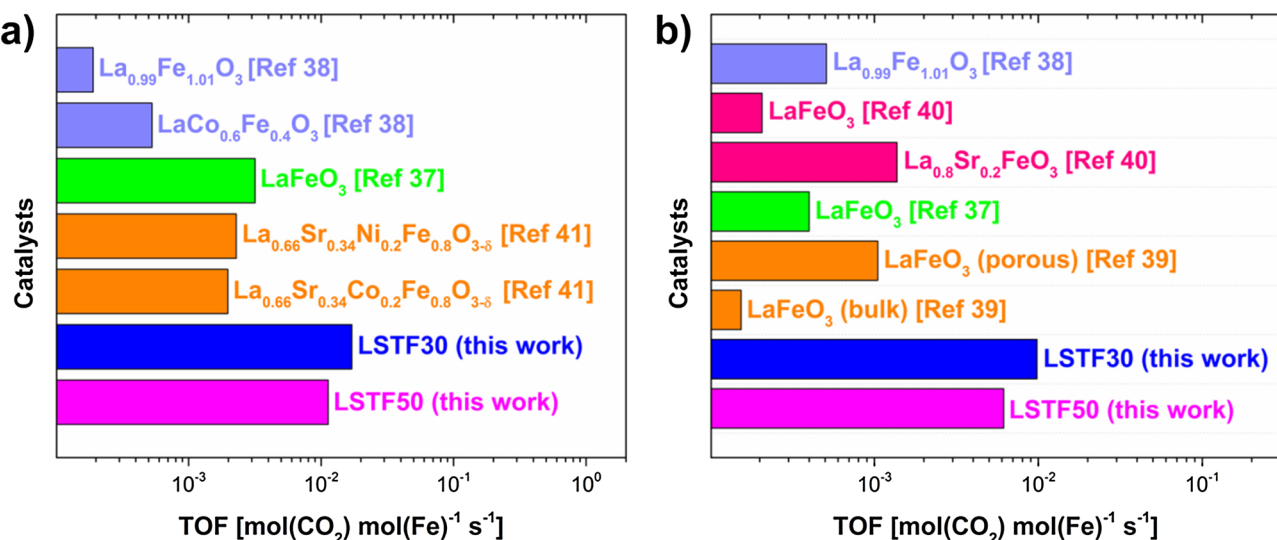


**Fig. 6.** Turnover frequencies (TOFs) of LSTF catalysts presented in this work compared with reported values for Fe-based catalysts in literature (a) for CH<sub>4</sub> oxidation at T = 560 °C (b) for CO oxidation at T = 300 °C. TOF values are normalized by total number of Fe species in catalyst.

those of other bulk and nanoporous iron-based perovskite catalysts in literature evidenced that our mesoporous solid solutions are by maximum 90 times more performing. This excellent result is not only related to the high surface area, but is more likely to rely on the mesoporous structure of the materials which combine large concentration of active sites, intimate gas-solid contact and short diffusion pathways for the oxygen species. In conclusion, we could demonstrate that such a catalyst design, in which both material composition and texture are finely controlled, shows prospective improvements for the catalytic performance of reforming catalysis using methane as well as for automobile exhaust control units.

## Acknowledgments

Sandra König, Uta Sazama and Isabelle Nevoigt of the University of Hamburg are gratefully acknowledged for the nitrogen physisorption, thermal analyses and powder X-ray diffraction measurements, respectively. Buğra Kayaalp thanks the MIN Graduate School International for the financial support during his stay at KAIST. Prof. Michael Fröba of the University of Hamburg is gratefully acknowledged for the support and the fruitful discussions. S. Lee, J. Seo and W. Jung were financially supported by the Korea Institute of Energy Technology Evaluation and Planning (KETEP) and the Ministry of Trade, Industry & Energy (MOTIE) of the Republic of Korea (No. 20174030201590 and No. 20173010032120).

## Appendix A. Supplementary data

Supplementary material related to this article can be found, in the online version, at doi:<https://doi.org/10.1016/j.apcatb.2018.12.077>.

## References

- [1] J.-J. Xu, D. Xu, Z.-L. Wang, H.-G. Wang, L.-L. Zhang, X.-B. Zhang, Synthesis of perovskite-based porous La<sub>0.75</sub>Sr<sub>0.25</sub>MnO<sub>3</sub> nanotubes as a highly efficient electrocatalyst for rechargeable lithium-oxygen batteries, *Angew. Chem. Int. Ed.* 52 (2013) 3887–3890, <https://doi.org/10.1002/anie.201210057>.
- [2] A.H. McDaniel, E.C. Miller, D. Arifin, A. Ambrosini, E.N. Coker, R. O’Hayre, W.C. Chueh, J. Tong, Sr- and Mn-doped LaAlO<sub>3-δ</sub> for solar thermochemical H<sub>2</sub> and CO production, *Energy Environ. Sci.* 6 (2013) 2424, <https://doi.org/10.1039/c3ee41372a>.
- [3] J. Suntivich, K.J. May, H.A. Gasteiger, J.B. Goodenough, Y. Shao-Horn, A perovskite oxide optimized for oxygen evolution catalysis from molecular orbital principles, *Science* 334 (80) (2011) 1383–1385, <https://doi.org/10.1126/science.1212858>.
- [4] S. Sengodan, S. Choi, A. Jun, T.H. Shin, Y.-W. Ju, H.Y. Jeong, J. Shin, J.T.S. Irvine, G. Kim, Layered oxygen-deficient double perovskite as an efficient and stable anode for direct hydrocarbon solid oxide fuel cells, *Nat. Mater.* 14 (2015) 205–209, <https://doi.org/10.1038/nmat4166>.
- [5] A. Kotarba, W. Bieniasz, M.J. Illán-gómez, Environmental Effect of potassium addition on catalytic activity of SrTiO<sub>3</sub> catalyst for diesel soot combustion, *Appl. Catal. B: Environ.* 101 (2011) 169–175, <https://doi.org/10.1016/j.apcatb.2010.09.018>.
- [6] S. Royer, D. Duprez, F. Can, X. Courtois, C. Batiot-Dupeyrat, S. Laassiri, H. Alamdari, Perovskites as substitutes of noble metals for heterogeneous catalysis: dream or reality, *Chem. Rev.* 114 (2014) 10292–10368, <https://doi.org/10.1021/cr500032a>.
- [7] M.M. Nair, F. Kleitz, S. Kaliaguine, Kinetics of methanol oxidation over mesoporous perovskite catalysts, *ChemCatChem* 4 (2012) 387–394, <https://doi.org/10.1002/cctc.201100356>.
- [8] M.M. Nair, S. Kaliaguine, F. Kleitz, Nanocast LaNiO<sub>3</sub> perovskites as precursors for the preparation of coke-resistant dry reforming catalysts, *ACS Catal.* (2014) 1–4.
- [9] B.E. Kayaalp, Y.J. Lee, A. Kornowski, S. Gross, M. D’Arienzo, S. Mascotto, Cooperative assembly synthesis of mesoporous SrTiO<sub>3</sub> with enhanced photocatalytic properties, *RSC Adv.* 6 (2016) 90401–90409, <https://doi.org/10.1039/C6RA13800D>.
- [10] X. Huang, G. Zhao, G. Wang, J.T.S. Irvine, Synthesis and applications of nanoporous perovskite metal oxides, *Chem. Sci.* 00 (2018) 1–15, <https://doi.org/10.1039/C7SC03920D>.
- [11] M. Sadakane, Takahito Asanuma, A. Jun Kubo, W. Ueda, Facile procedure to prepare three-dimensionally ordered macroporous (3DOM) perovskite-type mixed metal oxides by colloidal crystal templating method, *Chem. Mater.* 17 (2005) 3546–3551, <https://doi.org/10.1021/cm050511u>.
- [12] J. He, W. Zhou, J. Sunarso, X. Xu, Y. Zhong, Z. Shao, X. Chen, H. Zhu, 3D ordered macroporous SmCo<sub>3</sub>perovskite for highly active and selective hydrogen peroxide detection, *Electrochim. Acta* 260 (2018) 372–383, <https://doi.org/10.1016/j.electacta.2017.12.084>.
- [13] R.K.C. de Lima, M.S. Batista, M. Wallau, E.A. Sanches, Y.P. Mascarenhas, E.A. Urquiza-González, High specific surface area LaFeCo perovskites-synthesis by nanocasting and catalytic behavior in the reduction of NO with CO, *Appl. Catal. B Environ.* 90 (2009) 441–450, <https://doi.org/10.1016/j.apcatb.2009.04.004>.
- [14] A. Nenning, L. Volgger, E. Miller, L.V. Mogni, S. Barnett, J. Fleig, The electrochemical properties of Sr(Ti,Fe)O<sub>3-δ</sub> for anodes in solid oxide fuel cells, *J. Electrochim. Soc.* 164 (2017) F364–F371, <https://doi.org/10.1149/2.1271704jes>.
- [15] B. Koo, H. Kwon, Y. Kim, H.G. Seo, J.W. Han, W. Jung, Enhanced oxygen exchange of perovskite oxide surfaces through strain-driven chemical stabilization, *Energy Environ. Sci.* 11 (2018) 71–77, <https://doi.org/10.1039/c7ee00770a>.
- [16] W. Jung, H.L. Tuller, Investigation of cathode behavior of model thin-film SrTi<sub>1-x</sub>Fe<sub>x</sub>O<sub>3-δ</sub> (x = 0.35 and 0.5) mixed ionic-electronic conducting electrodes, *J. Electrochim. Soc.* 155 (2008), <https://doi.org/10.1149/1.2976212> B1194.
- [17] W. Jung, H. Tuller, Impedance study of SrTi<sub>1-x</sub>Fe<sub>x</sub>O<sub>3-δ</sub> (x = 0.05 to 0.80) mixed ionic-electronic conducting model cathode, *Solid State Ion.* 180 (2009).
- [18] W. Jung, H.L. Tuller, A new model describing solid oxide fuel cell cathode kinetics: model thin film SrTi<sub>1-x</sub>Fe<sub>x</sub>O<sub>3-δ</sub> mixed conducting Oxides-a case study, *Adv. Energy Mater.* 1 (2011) 1184–1191, <https://doi.org/10.1002/aenm.201100164>.
- [19] W. Jung, H.L. Tuller, Investigation of surface Sr segregation in model thin film solid oxide fuel cell perovskite electrodes, *Energy Environ. Sci.* 5 (2012) 5370–5378, <https://doi.org/10.1039/c1ee02762j>.
- [20] Y. Chen, W. Jung, Z. Cai, J.J. Kim, H.L. Tuller, B. Yildiz, Impact of Sr segregation on the electronic structure and oxygen reduction activity of SrTi<sub>1-x</sub>Fe<sub>x</sub>O<sub>3</sub> surfaces, *Energy Environ. Sci.* 5 (2012) 7979, <https://doi.org/10.1039/c2ee21463f>.
- [21] V.V. Kharton, A.P. Viskup, A.V. Kovalevsky, F.M. Figueiredo, J.R. Jurado, A.A. Yaremchenko, E.N. Naumovich, J.R. Fraile, Surface-limited ionic transport in perovskites Sr<sub>0.97</sub>(Ti,Fe,Mg)O<sub>3-δ</sub>, *J. Mater. Chem.* 10 (2000) 1161–1169, <https://doi.org/10.1039/a909710d>.
- [22] S. Steinsvik, R. Bugge, J. Gjønnes, J. Taftø, T. Norby, The defect structure of SrTi<sub>1-x</sub>Fe<sub>x</sub>O<sub>3-δ</sub> (x = 0–0.8) investigated by electrical conductivity measurements

and electron energy loss spectroscopy (EELS), *J. Phys. Chem. Solids* 58 (1997) 969–976, [https://doi.org/10.1016/S0022-3697\(96\)00200-4](https://doi.org/10.1016/S0022-3697(96)00200-4).

[23] J.R. Jurado, F.M. Figueiredo, B. Gharbage, J.R. Frade, Electrochemical permeability of  $\text{Sr}_{0.7}(\text{Ti},\text{Fe})\text{O}_{3-\delta}$  materials, *Solid State Ion.* 118 (1999) 89–97, [https://doi.org/10.1016/S0167-2738\(98\)00471-8](https://doi.org/10.1016/S0167-2738(98)00471-8).

[24] J.R. Jurado, F.M. Figueiredo, J.R. Frade, Overpotential terms on the electrochemical permeability of  $\text{Sr}_{0.97}(\text{Ti},\text{Fe})\text{O}_{3-\delta}$  materials, *Solid State Ion.* 122 (1999) 197–204, [https://doi.org/10.1016/S0167-2738\(99\)00061-2](https://doi.org/10.1016/S0167-2738(99)00061-2).

[25] Y. Takahashi, A. Kawahara, T. Suzuki, M. Hirano, W. Shin, Perovskite membrane of  $\text{La}_{1-x}\text{Sr}_x\text{Ti}_{1-y}\text{Fe}_y\text{O}_{3-\delta}$  for partial oxidation of methane to syngas, *Solid State Ion.* 181 (2010) 300–305, <https://doi.org/10.1016/J.SSI.2010.01.008>.

[26] S.J. Litzelman, A. Rothschild, H.L. Tuller, The electrical properties and stability of  $\text{SrTi}_{0.65}\text{Fe}_{0.35}\text{O}_{3-\delta}$  thin films for automotive oxygen sensor applications, *Sens. Actuators B Chem.* 108 (2005) 231–237, <https://doi.org/10.1016/J.SNB.2004.10.040>.

[27] A. Rothschild, S.J. Litzelman, H.L. Tuller, W. Meneskou, T. Schneider, E. Ivers-Tiffée, Temperature-independent resistive oxygen sensors based on  $\text{SrTi}_{1-x}\text{Fe}_x\text{O}_{3-\delta}$  solid solutions, *Sens. Actuators B Chem.* 108 (2005) 223–230, <https://doi.org/10.1016/J.SNB.2004.09.044>.

[28] K. Sahner, R. Moos, M. Matam, J.J. Tunney, M. Post, Hydrocarbon sensing with thick and thin film p-type conducting perovskite materials, *Sens. Actuators B Chem.* 108 (2005) 102–112, <https://doi.org/10.1016/J.SNB.2004.12.104>.

[29] K. Sahner, D. Schönauer, M. Matam, R. Moos, Selectivity enhancement of p-type semiconducting hydrocarbon sensors—the use of sol-precipitated nanopowders, *Sens. Actuators B Chem.* 130 (2008) 470–476, <https://doi.org/10.1016/J.SNB.2007.09.024>.

[30] T. Menke, R. Dittmann, P. Meuffels, K. Szot, R. Waser, Impact of the electroforming process on the device stability of epitaxial Fe-doped  $\text{SrTiO}_3$  resistive switching cells, *J. Appl. Phys.* 106 (2009), <https://doi.org/10.1063/1.3267485>.

[31] C. Lenser, Z. Connell, A. Kovács, R. Dunin-Borkowski, A. Köhl, R. Waser, R. Dittmann, Identification of screw dislocations as fast-forming sites in Fe-doped  $\text{SrTiO}_3$ , *Appl. Phys. Lett.* 102 (2013) 183504, <https://doi.org/10.1063/1.4804364>.

[32] D.P. Fagg, V.V. Kharton, J.R. Frade, L. Ferreira, Stability and mixed ionic – electronic conductivity of  $(\text{Sr},\text{La})(\text{Ti},\text{Fe})\text{O}_{3-\delta}$  perovskites, *Solid State Ion.* 156 (2003) 45–57, [https://doi.org/10.1016/S0167-2738\(02\)00257-6](https://doi.org/10.1016/S0167-2738(02)00257-6).

[33] X. Zhou, N. Yan, K.T. Chuang, J. Luo, Progress in La-doped  $\text{SrTiO}_3$  (LST)-based anode materials for solid oxide fuel cells, *RSC Adv.* 4 (2014) 118–131, <https://doi.org/10.1039/C3RA4266A>.

[34] K. Bin Yoo, G.M. Choi, Performance of La-doped strontium titanate (LST) anode on  $\text{LaGaO}_3$ -based SOFC, *Solid State Ion.* 180 (2009) 867–871, <https://doi.org/10.1016/j.ssi.2009.02.013>.

[35] J. Canales-Vázquez, J.C. Ruiz-Morales, D. Marrero-López, J. Peña-Martínez, P. Núñez, P. Gómez-Romero, Fe-substituted  $(\text{La},\text{Sr})\text{TiO}_3$  as potential electrodes for symmetrical fuel cells (SFCs), *J. Power Sources* 171 (2007) 552–557, <https://doi.org/10.1016/j.jpowsour.2007.05.094>.

[36] J.S. Yoon, Y.S. Lim, B.H. Choi, H.J. Hwang, Catalytic activity of perovskite-type doped  $\text{La}_{0.08}\text{Sr}_{0.92}\text{Ti}_{1-x}\text{M}_x\text{O}_{3-\delta}$  ( $\text{M} = \text{Mn, Fe, and Co}$ ) oxides for methane oxidation, *Int. J. Hydrogen Energy* 39 (2014) 7955–7962, <https://doi.org/10.1016/j.ijhydene.2014.03.008>.

[37] P. Ciambelli, S. Cimino, G. Lasorella, L. Lisi, S. De Rossi, M. Faticanti, G. Minelli, P. Porta, CO oxidation and methane combustion on  $\text{LaAl}_{1-x}\text{Fe}_x\text{O}_3$  perovskite solid solutions, *Appl. Catal. B Environ.* 37 (2002) 231–241.

[38] B. Levasseur, S. Kaliaguine, Effects of iron and cerium in  $\text{La}_{1-y}\text{Ce}_y\text{Co}_{1-x}\text{Fe}_x\text{O}_3$  perovskites as catalysts for VOC oxidation, *Appl. Catal. B Environ.* 88 (2009) 305–314, <https://doi.org/10.1016/j.apcatb.2008.11.007>.

[39] P. Xiao, L. Zhong, J. Zhu, J. Hong, J. Li, H. Li, Y. Zhu, CO and soot oxidation over macroporous perovskite  $\text{LaFeO}_3$ , *Catal. Today* 258 (2015) 660–667, <https://doi.org/10.1016/j.cattod.2015.01.007>.

[40] H. Einaga, Y. Nasu, M. Oda, H. Saito, Catalytic performances of perovskite oxides for CO oxidation under microwave irradiation, *Chem. Eng. J.* 283 (2016) 97–104, <https://doi.org/10.1016/j.cej.2015.07.051>.

[41] M. Alifanti, J. Kirchnerova, B. Delmon, D. Klvana, Methane and propane combustion over lanthanum transition-metal perovskites: role of oxygen mobility, *Appl. Catal. A Gen.* 262 (2004) 167–176, <https://doi.org/10.1016/j.apcata.2003.11.024>.

[42] X. Fan, Y. Wang, X. Chen, L. Gao, W. Luo, Y. Yuan, Z. Li, T. Yu, J. Zhu, Z. Zou, Facile method to synthesize mesoporous multimetal oxides ( $\text{ATiO}_3$ ,  $\text{A} = \text{Sr, Ba}$ ) with large specific surface areas and crystalline pore walls, *Chem. Mater.* 22 (2010) 1276–1278, <https://doi.org/10.1021/cm903303v>.

[43] S. Brunauer, P.H. Emmett, E. Teller, Adsorption of gases in multimolecular layers, *J. Am. Chem. Soc.* 60 (1938) 309–319 doi:citeulike-article-id:4074706.

[44] P.I. Ravikovich, A.V. Neimark, Characterization of micro- and mesoporosity in SBA-15 materials from adsorption data by the NLDFT method, *J. Phys. Chem. B* 105 (2001) 6817–6823, <https://doi.org/10.1021/jp010621u>.

[45] M. Thommes, K. Kaneko, A.V. Neimark, J.P. Olivier, F. Rodriguez-Reinoso, J. Rouquerol, K.S.W. Sing, Physisorption of gases, with special reference to the evaluation of surface area and pore size distribution (IUPAC Technical Report), *Pure Appl. Chem.* 87 (2015) 1051–1069, <https://doi.org/10.1515/pac-2014-1117>.

[46] M. Kakihana, M. Yoshimura, Synthesis and characteristics of complex multi-component oxides prepared by polymer complex method, *Bull. Chem. Soc. Jpn.* 72 (1999) 1427–1443, <https://doi.org/10.1246/bcsj.72.1427>.

[47] A. Rothschild, W. Meneskou, H.L. Tuller, E. Ivers-Tiffée, Electronic Structure, Defect chemistry, and transport properties of  $\text{SrTi}_{1-y}\text{Fe}_y\text{O}_{3-\delta}$  solid solutions, *Chem. Mater.* 18 (2006) 3651–3659, <https://doi.org/10.1021/cm052803x>.

[48] V. Metlenko, W. Jung, S.R. Bishop, H.L. Tuller, R.A. De Souza, Oxygen diffusion and surface exchange in the mixed conducting oxides  $\text{SrTi}_{1-y}\text{Fe}_y\text{O}_{3-\delta}$ , *Phys. Chem. Chem. Phys.* 18 (2016) 29495–29505, <https://doi.org/10.1039/C6CP05756J>.

[49] T.R. Clevenger, Effect of Fe4+ in the system  $\text{SrFeO}_3$ – $\text{SrTiO}_3$ , *J. Am. Ceram. Soc.* 46 (1963) 207–210, <https://doi.org/10.1111/j.1151-2916.1963.tb19773.x>.

[50] A.A. Leontiou, A.K. Ladavos, A.E. Giannakas, T.V. Bakas, P.J. Pomonis, A comparative study of substituted perovskite-type solids of oxidic  $\text{La}_{1-x}\text{Sr}_x\text{FeO}_{3-\delta}$  and chlorinated  $\text{La}_{1-x}\text{Sr}_x\text{FeO}_{3-\delta}\text{Cl}_\alpha$  form: catalytic performance for  $\text{CH}_4$  oxidation by O, *J. Catal.* 251 (2007) 103–112, <https://doi.org/10.1016/j.jcat.2007.07.012>.

[51] A. Rothschild, Y. Komen, A. Levakov, N. Ashkenasy, Y. Shapira, Electronic and transport properties of reduced and oxidized nanocrystalline  $\text{TiO}_2$  films, *Appl. Phys. Lett.* 82 (2003) 574, <https://doi.org/10.1063/1.1539556>.

[52] N.H. Perry, D. Pergolesi, S.R. Bishop, H.L. Tuller, Defect chemistry and surface oxygen exchange kinetics of La-doped  $\text{Sr}(\text{Ti},\text{Fe})\text{O}_{3-\alpha}$  in oxygen-rich atmospheres, *Solid State Ion.* 273 (2015) 18–24, <https://doi.org/10.1016/j.ssi.2014.09.013>.

[53] L. Xi, L. Xiaoxun, X. Baokun, Z. Miyu, XPS study of adsorbed oxygen of nanocrystalline  $\text{LaFeO}_3$  materials, *J. Alloys Compd.* 186 (1992) 315–319, [https://doi.org/10.1016/0925-8388\(92\)90018-5](https://doi.org/10.1016/0925-8388(92)90018-5).

[54] E. García-López, G. Marci, F. Puleo, V. La Parola, L.F. Liotta,  $\text{La}_{1-x}\text{Sr}_x\text{Co}_{1-y}\text{Fe}_{y}\text{O}_{3-\delta}$  perovskites: preparation, characterization and solar photocatalytic activity, *Appl. Catal. B Environ.* 178 (2015) 218–225, <https://doi.org/10.1016/j.apcatb.2014.09.014>.

[55] K. Ji, H. Dai, J. Deng, L. Zhang, F. Wang, H. Jiang, C.T. Au, Three-dimensionally ordered macroporous  $\text{SrFeO}_3-\delta$  with high surface area: active catalysts for the complete oxidation of toluene, *Appl. Catal. A Gen.* 425–426 (2012) 153–160, <https://doi.org/10.1016/j.apcata.2012.03.013>.

[56] H. Falcón, J.A. Barbero, J.A. Alonso, M.J. Martínez-Lope, J.L.G. Fierro,  $\text{SrFeO}_{3-\delta}$  perovskite oxides: chemical features and performance for methane combustion, *Chem. Mater.* 14 (2002) 2325–2333, <https://doi.org/10.1021/cm011292l>.

[57] M.S.S. Khine, L. Chen, S. Zhang, J. Lin, S.P. Jiang, Syngas production by catalytic partial oxidation of methane over  $(\text{La}_{0.7}\text{A}_{0.3})\text{BO}_3$  ( $\text{A} = \text{Ba, Ca, Mg, Sr, and B} = \text{Cr or Fe}$ ) perovskite oxides for portable fuel cell applications, *Int. J. Hydrogen Energy* 38 (2013) 13300–13308, <https://doi.org/10.1016/j.ijhydene.2013.07.097>.

[58] Z. Zhao, X. Yang, Y. Wu, Comparative study of Nickel-based perovskite-like mixed oxide catalysts for direct decomposition of NO, *Appl. Catal. B Environ.* 8 (1996) 281–297, [https://doi.org/10.1016/0926-3373\(95\)00067-4](https://doi.org/10.1016/0926-3373(95)00067-4).

[59] L. Karanovic, S. Petrović, V. Donduš, D. Paneva, I. Mitov, V. Rakic,  $\text{LaMO}_3$  ( $\text{M} = \text{Mg, Ti, Fe}$ ) perovskite type oxides : preparation, characterization and catalytic properties in methane deep oxidation, *Appl. Catal. B: Environ.* 79 (2008) 186–198, <https://doi.org/10.1016/j.apcatb.2007.10.022>.

[60] J. Zhu, D. Xiao, J. Li, X. Yang, Perovskite-like mixed oxides ( $\text{LaSrMn}_{1-x}\text{Ni}_{x}\text{O}_{4+\delta}$ ,  $0 \leq x \leq 1$ ) as catalyst for catalytic NO decomposition: TPD and TPR studies, *Catal. Letters* 129 (2009) 240–246, <https://doi.org/10.1007/s10562-008-9807-8>.

[61] G. Pecchi, M.G. Jiliberto, A. Buljan, E.J. Delgado, Relation between defects and catalytic activity of calcium doped  $\text{LaFeO}_3$  perovskite, *Solid State Ion.* 187 (2011) 27–32, <https://doi.org/10.1016/j.ssi.2011.02.014>.

[62] H. Arai, T. Yamada, K. Eguchi, T. Seiyama, Catalytic combustion of methane over various perovskite-type oxides, *Appl. Catal.* 26 (1986) 265–276, [https://doi.org/10.1016/S0166-9834\(00\)82556-7](https://doi.org/10.1016/S0166-9834(00)82556-7).

[63] P. Granger, V.I. Parvulescu, S. Kaliaguine, W. Prellier, *Perovskites and Related Mixed Oxides: Concepts and Applications*, John Wiley & Sons, 2016.

[64] V.C. Belessi, A.K. Ladavos, G.S. Armatas, P.J. Pomonis, Kinetics of methane oxidation over  $\text{La-Sr-Ce-Fe-O}$  mixed oxide solids, *Phys. Chem. Chem. Phys.* 3 (2001) 3856–3862, <https://doi.org/10.1039/b103426j>.